

ESTIMATION OF UNCERTAINTIES OF FULL MOMENT TENSORS

Carl Tape, et al.

University of Alaska Fairbanks
Geophysical Institute
903 Koyukuk Dr.
Fairbanks, AK 99775

06 October 2017

Final Report

APPROVED FOR PUBLIC RELEASE; DISTRIBUTION IS UNLIMITED.



**AIR FORCE RESEARCH LABORATORY
Space Vehicles Directorate
3550 Aberdeen Ave SE
AIR FORCE MATERIEL COMMAND
KIRTLAND AIR FORCE BASE, NM 87117-5776**

DTIC COPY

NOTICE AND SIGNATURE PAGE

Using Government drawings, specifications, or other data included in this document for any purpose other than Government procurement does not in any way obligate the U.S. Government. The fact that the Government formulated or supplied the drawings, specifications, or other data does not license the holder or any other person or corporation; or convey any rights or permission to manufacture, use, or sell any patented invention that may relate to them.

This report was cleared for public release by the RD/RV Communications Office and is available to the general public, including foreign nationals. Copies may be obtained from the Defense Technical Information Center (DTIC) (<http://www.dtic.mil>).

AFRL-RV-PS-TR-2017-0186 HAS BEEN REVIEWED AND IS APPROVED FOR
PUBLICATION IN ACCORDANCE WITH ASSIGNED DISTRIBUTION STATEMENT.

//SIGNED//

Dr. Frederick Schult
Program Manager, AFRL/RVBYE

//SIGNED//

Dr. Thomas R. Caudill, Acting Chief
AFRL Battlespace Environment Division

This report is published in the interest of scientific and technical information exchange, and its publication does not constitute the Government's approval or disapproval of its ideas or findings.

REPORT DOCUMENTATION PAGE

Form Approved
OMB No. 0704-0188

Public reporting burden for this collection of information is estimated to average 1 hour per response, including the time for reviewing instructions, searching existing data sources, gathering and maintaining the data needed, and completing and reviewing this collection of information. Send comments regarding this burden estimate or any other aspect of this collection of information, including suggestions for reducing this burden to Department of Defense, Washington Headquarters Services, Directorate for Information Operations and Reports (0704-0188), 1215 Jefferson Davis Highway, Suite 1204, Arlington, VA 22202-4302. Respondents should be aware that notwithstanding any other provision of law, no person shall be subject to any penalty for failing to comply with a collection of information if it does not display a currently valid OMB control number. PLEASE DO NOT RETURN YOUR FORM TO THE ABOVE ADDRESS.

1. REPORT DATE (DD-MM-YYYY) 06-10-2017	2. REPORT TYPE Final Report	3. DATES COVERED (From - To) 17 Jun 2015 – 17 Jun 2017
4. TITLE AND SUBTITLE Estimation of Uncertainties of Full Moment Tensors		5a. CONTRACT NUMBER FA9453-15-C-0063
		5b. GRANT NUMBER
		5c. PROGRAM ELEMENT NUMBER 62601F
6. AUTHOR(S) Carl Tape, Walter Tape, Celso Alvizuri, and Vipul Silwal		5d. PROJECT NUMBER 1010
		5e. TASK NUMBER PPM00019619
		5f. WORK UNIT NUMBER EF127882
7. PERFORMING ORGANIZATION NAME(S) AND ADDRESS(ES) University of Alaska Fairbanks Geophysical Institute 903 Koyukuk Dr. Fairbanks, AK 99775		8. PERFORMING ORGANIZATION REPORT NUMBER
9. SPONSORING / MONITORING AGENCY NAME(S) AND ADDRESS(ES) Air Force Research Laboratory Space Vehicles Directorate 3550 Aberdeen Avenue SE Kirtland AFB, NM 87117-5776		10. SPONSOR/MONITOR'S ACRONYM(S) AFRL/RVBYE
		11. SPONSOR/MONITOR'S REPORT NUMBER(S) AFRL-RV-PS-TR-2017-0186

12. DISTRIBUTION / AVAILABILITY STATEMENT

Approved for public release; distribution is unlimited. (RDMX-18-17140 dtd 29 Mar 2018)

13. SUPPLEMENTARY NOTES

14. ABSTRACT

A seismic moment tensor is a 3×3 symmetric matrix that provides a compact representation of a seismic source. We develop an algorithm to estimate moment tensors and their uncertainties from observed seismic data. For a given event, the algorithm performs a grid search over the six-dimensional space of moment tensors by generating synthetic waveforms for each moment tensor and then evaluating a misfit function between the observed and synthetic waveforms. 'The' moment tensor M_0 for the event is then the moment tensor with minimum misfit. To describe the uncertainty associated with M_0 , we first convert the misfit function to a probability function. The uncertainty, or rather the confidence, is then given by the 'confidence curve' $P(V)$, where $P(V)$ is the probability that the true moment tensor for the event lies within the neighborhood of M that has fractional volume V . The area under the confidence curve provides a single, abbreviated 'confidence parameter' for M_0 . We apply the method to data from events in different regions and tectonic settings: 63 small ($M_w < 2.5$) events at Uturuncu volcano in Bolivia, 21 moderate ($M_w > 4$) earthquakes in the southern Alaska subduction zone, and 12 earthquakes and 17 nuclear explosions at the Nevada Test Site. Characterization of moment tensor uncertainties puts us in better position to discriminate among moment tensor source types and to assign physical processes to the events.

15. SUBJECT TERMS

seismic moment tensor, seismic source, moment tensor uncertainty

16. SECURITY CLASSIFICATION OF:			17. LIMITATION OF ABSTRACT Unlimited	18. NUMBER OF PAGES 30	19a. NAME OF RESPONSIBLE PERSON Dr. Frederick Schult
a. REPORT Unclassified	b. ABSTRACT Unclassified	c. THIS PAGE Unclassified			19b. TELEPHONE NUMBER (include area code)

This page is intentionally left blank.

Table of Contents

1. Summary	1
2. Introduction.....	1
3. Technical Approach.....	3
4. Results.....	5
5. Discussion.....	7
6. Conclusions.....	9
References.....	21

List of Figures

1.	Fundamental lune for moment tensor source types	11
2.	Locator maps for study regions.....	12
3.	Waveform fits for HOYA nuclear test.....	13
4.	Uncertainty summary for HOYA nuclear test	15
5.	Waveform fits for four nuclear explosions	17
6.	Lune plots for four nuclear explosions	18
7.	Surface wave time shifts for two stations	19
8.	The influence of body waves on lune plots	19
9.	Moment tensor catalogs plotted on the lune	20

1. SUMMARY

A seismic moment tensor is a 3×3 symmetric matrix that provides a compact representation of a seismic source. We develop an algorithm to estimate moment tensors and their uncertainties from observed seismic data. For a given event, the algorithm performs a grid search over the six-dimensional space of moment tensors by generating synthetic waveforms for each moment tensor and then evaluating a misfit function between the observed and synthetic waveforms. ‘The’ moment tensor M_0 for the event is then the moment tensor with minimum misfit. To describe the uncertainty associated with M_0 , we first convert the misfit function to a probability function. The uncertainty, or rather the confidence, is then given by the ‘confidence curve’ $P(V)$, where $P(V)$ is the probability that the true moment tensor for the event lies within the neighborhood of M_0 that has fractional volume V . The area under the confidence curve provides a single, abbreviated ‘confidence parameter’ for M_0 . We apply the method to data from events in different regions and tectonic settings: 63 small ($M_w < 2.5$) events at Uturuncu volcano in Bolivia, 21 moderate ($M_w > 4$) earthquakes in the southern Alaska subduction zone, and 12 earthquakes and 17 nuclear explosions at the Nevada Test Site. Characterization of moment tensor uncertainties puts us in better position to discriminate among moment tensor source types and to assign physical processes to the events.

2. INTRODUCTION

2.1 Background on moment tensor source type

The moment tensor is an expression of the source for small to moderate seismic events. Mathematically, it is a 3×3 symmetric matrix, and the space of moment tensors is therefore six-dimensional. Traditionally, moment tensors have often been constrained to be deviatoric, meaning that their trace should be zero, in which case only a subspace of the six-dimensional space is used. In the past two decades, however, several authors have argued against such constraints, especially when the seismic events under consideration are not true tectonic earthquakes but rather are associated with volcanic or geothermal activity, glaciers, mine collapses, hydraulic fracturing, or explosions (Ford et al., 2009, 2010); see review in Tape and Tape (2013, Figures 14 and S14).

The emphasis within our proposed study is on the uncertainties of moment tensors, notably those associated with the source type. The source type refers to two coordinates that characterize the isotropic and CLVD components within a moment tensor. These components are provided by the lune latitude (δ) and lune longitude (γ), which are simply angular measures in eigenvalue space. The ‘fundamental lune’ is a sector of this 3D eigenvalue space that covers all possible moment tensor source types (cf. Riedesel and Jordan, 1989). The center of the lune is a double couple $(1, 0, -1)$, while the top and bottom of the lune are isotropic points (Figure 1). The lune can be partitioned into four regions by three arcs at $\lambda_3 = 0$, $\lambda_2 = 0$, and $\lambda_1 = 0$. The distance on the lune is the natural measure of distance between moment tensors. For example, for two moment tensors with the same basis U , the angle between lune points is the same as the angle between the

moment tensors in matrix space (Tape and Tape, 2013). The ‘amount’ of double couple or CLVD or isotropic part within a moment tensor is calculated as the angular distance from a moment tensor to one of these points on the lune.

The lune—by which we mean the eigenvalue space for moment tensors—provides clarity to some convoluted areas of moment tensor literature. For example, there are three different published formulas for the ‘percent’ of ISO, DC, and CLVD from a given moment tensor; furthermore, two—not three—parameters should be needed to characterize moment tensor source type. And there are at least four published equations for obtaining the seismic moment from a given moment tensor; see comparison in Tape and Tape (2012b, Figure 13). Thus it is challenging to compare results across studies when so many different methods are used to represent the solutions. Finally, it turns out that alternate representations for source type—notably the T-k plot of Hudson et al. (1989)—turn out to be underlain by unphysical assumptions about uniformity of source types (Tape and Tape, 2012b). The lune provides a natural framework that leads to simpler expressions for characterizing moment tensors.

Three relevant topics from Tape and Tape (2013) are (1) the calculation of volume change, (2) the lack of justification for the deviatoric constraint, and (3) the interpretation of multiple events. Tape and Tape (2013) called into question the ubiquitous (in the published literature) interchangeability of ‘isotropic component’ and ‘volumetric component’. In fact, the volume change component varies with longitude—not latitude—on the lune. We also questioned the continued use of the deviatoric constraint within operational moment tensor codes: this constraint is only needed because it is difficult to constrain uncertainties. (In fact, from a theoretical standpoint, the constant- v constraint would be more appropriate than the zero-trace constraint (Minson et al., 2007; Tape and Tape, 2012a).) We also introduced a generic ‘two-source model’ that could produce a wide spread of full moment tensors on the lune that is seen in the literature. But in general we caution against invoking multiple events or using decompositions, as the classical model for moment tensors—an oblique opening (or closing) crack within a medium with Poisson parameter v —provides the simplest interpretation for full moment tensors (Tape and Tape, 2013). As noted in Tape and Tape (2013), we must have uncertainty estimates for published moment tensors in order to test physical models for moment tensors.

2.2 Theoretical development and application for moment tensor uncertainties

In the past decade, efforts have been made to characterize uncertainties of moment tensors. Some studies have estimated the uncertainties by repeatedly solving for M_0 using different subsets of data (bootstrapping or related Monte Carlo approaches). Other studies have provided a view of how the misfit function varied over the full space of moment tensor source types (Ford et al., 2010; Alvizuri and Tape, 2016). To our knowledge, Stahler and Sigloch (2014) is the only study to have formally accounted for uncertainties, by generating moment tensor samples of a posterior probability density. This was made possible by using a uniform distribution of moment tensors; we use an alternative uniform distribution in our study Tape and Tape (2015a).

The goal of this study is to estimate moment tensor uncertainties for three sets of previously studied events: 21 Alaska earthquakes, 63 volcanic events, and 29 events from

the Nevada Test Site. Following Tape and Tape (2016), we represent moment tensor uncertainties in the form of a confidence curve that expresses the concentration of probability in moment tensor space near M_0 . We build upon three recent studies: Tape and Tape (2016), which established the theory for confidence curves; Silwal and Tape (2016), which estimated confidence curves for double couple moment tensors; and Alvizuri and Tape (2016), which estimated a catalog of full moment tensors for volcanic events. In our examination of earthquakes and nuclear explosions from the Nevada Test Site, we use the exact same events as in Ford et al. (2009). In comparison with the approach of Ford et al. (2009), we use more stations, body waves (in addition to surface waves), a broader bandpass for surface waves ($T = 7\text{--}50$ s), and an alternative characterization of moment tensor uncertainties.

2.3 Summary of project publications

Our project resulted in eight publications, including three publications in peer-reviewed journals:

- *Journal publications*: Tape and Tape (2015a, 2016, 2017)
- *Journal publication in preparation*: Alvizuri et al. (2017, in prep.)
- *Abstracts*: Tape and Tape (2015b); Alvizuri et al. (2016, 2017); Tape (2017a)
- *Technical reports*: Tape (2017b)

We expect to submit a fourth publication (Alvizuri et al., 2017, in prep.) by December 2017. Our final report focuses on the unsubmitted manuscript, since full details of the other work can be found within the three published papers.

3. TECHNICAL APPROACH

3.1 Data

We examine events from three previous studies: 21 earthquakes in southern Alaska (tab. 4, Silwal and Tape, 2016), 63 events at Uturuncu volcano in Bolivia (tab. 4, Alvizuri and Tape, 2016), and 29 earthquakes and nuclear tests at the Nevada Test Site (tab. 1 of Ford et al., 2009). Figure 1 shows the three regions and the stations used within the moment tensor inversions.

For the Alaska and Uturuncu data sets, all waveforms are openly available from the IRIS Data Management Center. For the Nevada Test Site events, the waveforms are openly available from IRIS and the Northern California Data Center, while other waveforms are from Walter et al. (2006).

All waveforms were downloaded and processed using ObsPy, a python-based package for seismology. The processing steps for each event were: (1) obtain three-component waveforms and metadata from the IRIS (Incorporated Research Institutions for Seismology) Data Management Center, the Northern California Earthquake Data Center (NCEDC), or Walter et al. (2006); the time interval is 100~s before the origin time to 600~s after the origin time, (2) remove instrument response using an acausal Butterworth filter, (3) using the source-station azimuth and the sensor orientation angle, rotate horizontal components to radial and transverse directions. Additional processing

steps, such as cutting time windows and additional bandpass filtering, were applied during the moment tensor inversions.

We use high-frequency P waves for the Uturuncu and NTS events. Within the misfit function, described next, we make waveform measurements between observed and synthetic P waves. These measurements are more reliable when we align the P waves on the observed P arrival time.

3.2 Methods

Seismic moment tensor inversion requires specifying a misfit function between observed seismograms and synthetic (or ‘modeled’) seismograms. Synthetic seismograms are calculated using a model of the source---in our case, a moment tensor---and a model of Earth’s structure---in our case, a layered model. We calculate synthetic seismograms for a range of source depths and source-station distances using the frequency-wavenumber method. The source origin times and hypocenters are assumed to be fixed.

The misfit function we use, from Zhu and Helmberger (1996), measures integrated differences between observed and synthetic velocity seismograms within five time windows: P wave on vertical and radial components, Rayleigh wave on vertical and radial components, and Love wave on transverse component. Prior to calculating the waveform difference, we allow the synthetic seismograms to be shifted in time to maximize the cross-correlation with observed seismograms. For each station, three time shifts are allowed, for the P, Rayleigh, and Love waves. These different time shifts are allowed because these waves are sensitive to different parts of Earth structure. By allowing for different time shifts, we are recognizing that our layered Earth structural models cannot adequately predict the traveltimes for seismic waves. Additional discussion of time shifts can be found in Silwal and Tape (2016).

For our moment tensor inversions, we use the ‘cut-and-paste’ (CAP) code of Zhu and Helmberger (1996) and Zhu and Ben-Zion (2013), with some modifications. For the misfit function we use an L1 norm Silwal and Tape (2016), and we incorporate the number of misfitting polarities into the waveform-based misfit function. We also use an efficient grid search over moment tensor space, described below.

3.3 Moment tensor source type

The source type of a seismic moment tensor is represented by two parameters that are derived directly from the three eigenvalues of the 3×3 moment tensor. The norm of the eigenvalue triple provides the magnitude of the moment tensor, leaving two free parameters to define the source type. In the same year, Hudson et al. (1989) introduced the T-k source type plot, while Riedesel and Jordan (1989) introduced a representation of source types on a sphere. The motivation for the 2D T-k plot was to achieve uniform distribution of moment tensors—however uniformity was assumed to apply to a cube in eigenvalue space, an assumption with no reasonable justification. Chapman and Leaney (2012) dismissed the fundamental assumption of the T-k representation, and they advocated using the eigensphere, following Riedesel and Jordan (1989). Tape and Tape provided a geometrical framework for using the eigensphere for representing source type, with the two parameters being lune longitude—quantifying the CLVD component—and

lune latitude—quantifying the isometric component. Tape and Tape (2012b) compared the source type representations of T-k and the lune, showing the problems associated with the cube assumption underlying the T-k representation.

As pointed out by several authors, including Hudson et al. (1989), Ford et al. (2010), and Chapman and Leaney (2012), neither the source type plots of T-k nor the lune provide a uniform distribution of moment tensors. Toward the boundary of the source type plots, the eigenvalues become degenerate and the moment tensors are similar to each other, irrespective of orientation. Tape and Tape (2015) introduced a parameterization of source type that provides uniform moment tensors: “The parametrization is uniform, in the sense that equal volumes in the coordinate domain of the parametrization correspond to equal volumes of moment tensors.” (Tape and Tape, 2015, used u and v , but in our work we have used w instead of u ; u is similar to colatitude, while w is similar to latitude.) Tape and Tape (2015) discuss the vw rectangle in comparison with the lune:

“The homogeneous probability for moment tensors is the probability in which equal volumes of moment tensors are equally likely. If we are committed to the homogeneous probability as the a priori probability for moment tensors, then the lune is not the right place to display eigenvalue triples λ , if the display is intended to reveal non-uniformities. (For example, a tendency for the λ s to favour the center of the lune does not mean that we are dealing with a double couple.) Rather the eigenvalue triples should be displayed in the uv coordinate domain Q , since the a priori probability density for eigenvalue triples in Q is constant. When not specifically trying to convey or detect non-uniformities, however, we recommend the lune, since, after all, the lune is exactly the set of ordered and normalized eigenvalue triples.”

We see merits to both the lune and the vw plot. We see no justification for the underlying assumption associated with the T-k plot; nevertheless, the plot still serves the purpose of conveying the moment tensor source type.

4. RESULTS

4.1 Nevada earthquakes

The Little Skull Mountain earthquake of 1992-06-29 occurred inside the Nevada Test Site (Figure 2) and is the largest earthquake analyzed by Ford et al. (2009). It is notable for its size ($M_w > 5$) and its occurrence near Yucca Mountain, which, at the time, was under consideration as storage site for nuclear waste. Table 1 of Lohman et al. (2002) summarizes several studies of the source parameters of the Little Skull Mountain earthquake.

Our moment tensor inversions for the Little Skull Mountain earthquake used 15 broadband stations. For our first inversion, we assume a double couple moment tensor and include body waves (filtered 1–4 s) and surface waves (filtered 10–50 s). We first perform a coarse search over magnitude, depth, strike, dip, and rake, to determine the best-fitting depth and magnitude. The depth search over full moment tensor space provides similar results, with a best-fitting depth of 10 km. We use 10 km for the

estimated depth, based on consensus from previous studies, several of which are more sensitive to depth estimation (Lohman et al., 2002).

With the depth and magnitude fixed, we then perform a fine grid search over the space of strike, dip, and rake. Synthetic seismograms from the 1D model are able to fit the main surface wave arrivals on the data, but they are not able to fit the complexities caused by 3D structure, such as for paths across the San Joaquin Valley and Sierra Nevada. These effects are diminished when filtering seismograms with a larger minimum period (such as 20 s instead of 10 s).

Our misfit analysis of double couple moment tensors was presented in Silwal and Tape (2016) for Alaska earthquakes. Application to the Little Skull Mountain earthquake provides a sampling of 20 beachballs from the posterior distribution; we see that a normal-fault mechanism is preferred, but that the data allow for some notable deviations. An optimal confidence curve is one that has a steep slope at the origin and then rises all the way to $P(V) \sim 1$, such that $P(V)$ makes the shape of a Γ . For the Little Skull Mountain earthquake, the confidence curve has a steep slope at the origin but then reveals a more gradual rise, indicating that the probability for the solution is encountered gradually as one moves away from the global minimum moment tensor solution.

The full moment tensor solution for Little Skull Mountain reveals a minor improvement of waveform fits (VR 30.6 vs 28.2). Our initial misfit analysis of full moment tensors was presented in Alvizuri and Tape (2016) for events at Uturuncu volcano. Application to the Little Skull Mountain earthquake reveals a best-fitting solution that is close to the deviatoric arc, with lune longitude $\gamma = 14^\circ$ and lune latitude 3° .

Within the moment tensor inversions, time shifts are applied to the synthetic waveforms in an attempt to account for the approximateness of our layered velocity model. The time shifts provide a perspective on potential cycle-skipping of waveform fits, since stations in the same azimuth should have time shifts with the same sign.

The time shifts exhibit systematic variations with azimuth that we attribute to differences in 3D structure. The sign discrepancy between time shifts for Love and Rayleigh waves suggests the presence of crustal anisotropy or that the 1D model needs to be adjusted in the shallowest layer, where the Love and Rayleigh waves have differing sensitivities. The plots also reveal stations that are nodal to the mechanism. At these stations, the P and Rayleigh waves can be low amplitude and possibly distorted by 3D structure effects.

4.2 Nevada nuclear tests

Following Ford et al. (2009), we use the 1991-09-14 HOYA nuclear test to illustrate the waveform fits and misfit analysis. For HOYA we use 14 stations and filter surface waves at 10–50 s and body waves at high frequencies (0.8–10 Hz). For the LLNL stations we use the ‘HF’ waveforms for the body waves and ‘LF’ waveforms for the surface waves. (These waveforms are recorded by different sensors.) For the body waves, we align the synthetic P waves on the observed P onset times and then allow a time shift of only 0.5 s.

The waveform fits and misfit analysis for HOYA are shown in Figures 3 and 4. The best-fitting moment tensor is at $(5^\circ, 76^\circ)$ on the lune, within the isotropic region defined by all-positive eigenvalues. The region of lowest fit is tightly constrained around the best-

fitting solution, but there is also a weak local minimum in that negative isotropic region (Figure 4) arising from cycle-skipping.

We calculate moment tensor solutions for all 32 events from Ford et al. (2009). Lune plots and waveform fits for four nuclear explosions are shown in Figures 5 and 6. The events of Ford et al. (2009) are represented as beachballs on the lune in Figure 9a. We also plot the beachballs on the vw rectangle, which has an advantage over the lune in that distances on the plot better reflect distances between moment tensors. As an example, the 17 explosions from Ford et al. (2009) are spread out on the lune but are close together on the rectangle, indicating that the moment tensors are quantifiably very similar to each other. Our moment tensor solutions for the 32 events are shown in Figure 9b.

4.3 Uturuncu volcanic events

We reproduce the results from Alvizuri and Tape (2016), but using a modified misfit function. Previously we excluded any moment tensor that had any disagreement between its predicted first-motion polarities and the observed first-motion polarities. The modified misfit function balances the polarity misfit with the waveform misfit. This means that the misfit function is plotted on the entire lune, rather than on a subregion, as in Alvizuri and Tape (2016).

Figure 9c shows the full moment tensor catalog for 63 small ($M_w < 3$) events at Uturuncu volcano. Most events in the catalog have a positive isotropic component ($\delta > 0^\circ$). We show the beachballs on a plot of the vw rectangle, which is more appropriate than the lune when the intent is to represent distances in moment tensor space. All-outward beachballs (with all positive eigenvalues) are quite similar to each other; as we might expect, they occupy a much larger region on the lune than they do on the vw rectangle.

4.4 Alaska earthquakes

We apply the analysis of Alvizuri and Tape (2016) to the 21 earthquakes of Silwal and Tape (2016). No first-motion polarities were used, so the misfit function uses only waveform differences. Figure 9d shows the full moment tensor solutions on the lune and on the vw rectangle. While some earthquakes exhibit a possibly spurious, negative isotropic component, most events are quite close to the double couple at the center of the lune.

5. DISCUSSION

Earthquakes are useful for calibrating the results from non-earthquake events, such as nuclear explosions. Importantly, the full moment tensor inversions for earthquakes need to be performed with conditions that are as close to possible to those of the non-earthquake events, notably: same stations, same time period (meaning same station metadata), similar epicentral region (similar paths). This was the motivation behind the event selection in Ford et al. (2009).

Earthquake mechanisms estimated as full moment tensors tend to cluster near the double couple region of source type space, as we might hope. However, the spread of best-fitting moment tensors can deviate significantly from the ideal double couple, as

shown in Boyd et al. (2015) for a set of 828 events in the Berkeley Seismological Laboratory catalog. The Berkeley moment tensor solutions typically use <8 stations and are based on low-pass-filtered surface waves. By comparison, our full moment tensor analysis of 21 Alaska earthquakes uses dozens of stations and also includes body waves. The moment tensors are more tightly clustered around the double couple at the center of the lune (Figure 9d). This suggests that improved data coverage and use of body waves can diminish the spread in source types that are observed for sets of earthquakes.

For the moment tensor inversions in this study we have included waveform fits for body waves. To examine the influence of body waves, we performed separate inversions with body waves only, surface waves only, and both combined. Results for the Little Skull Mountain earthquake and the HOYA nuclear test are shown in Figure 8. For the Little Skull Mountain earthquake we see that all three mechanisms are notably different, though they all share a white central region and solid regions to the northwest and southeast. The body+surf lune plot (Figure 8c) appears to be a blend of the lune plots for the body-only (Figure 8a) and surface-only (Figure 8b) cases. Note that the magnitude estimate from body waves only is lower than the overall estimate (Mw 4.9 vs Mw 5.2).

For HOYA, the lune plot for body+surf (Figure 8f) reveals multiple good-fitting regions, some of which are present in the body-only (Figure 8d) and surface-only (Figure 8e) lune plots. Although first-motion polarities are not used within the inversion, each mechanism predicts outward first-motions at all stations.

It is possible that the mechanisms obtained from high-frequency body waves could differ from the mechanisms obtained from long-period surface waves. This could arise from time-dependent complexity in the source process, whereby the initial slip is responsible for the body waves and later, longer-duration slip is responsible for generating surface waves. Therefore we must be careful in interpreting differences in Figure 8, since some could be real, rather than caused by errors in modeling or data.

Our magnitude estimates for the Little Skull Mountain earthquake and for HOYA are lower than those in the published literature. Our Mw 5.2 estimate for Little Skull Mountain compares with Mw 5.6 from Lohman et al. (2002) and Ford et al. (2009) and Mw 5.7 from the GCMT catalog. Further work, including testing of different velocity models and attenuation models, is needed to examine this discrepancy.

The application of time shifts to synthetic seismograms in moment tensor inversions is a widely used practice that can be both subtle and dangerous. As an extreme example, the moment tensor $-M_0$ will exhibit the same relative variations in amplitudes as the best-fitting moment tensor M_0 . While the inclusion of first-motion polarity measurements can distinguish between these extreme cases, there are other cases that are difficult. With only ten or so waveforms, as in the case of the NTS events, a single misaligned waveform can influence the solution. One challenge is that the prospects of cycle skipping—misalignment of the synthetic wave with the observed wave—increase as we decrease the period content.

The best approach to eliminating time shifts would be to use a 3D velocity model that accurately predicts the arrival times of all waves used in the moment tensor inversion. For us, this would require accurate prediction of the seismic wavefield for periods >1 s. Such a regional model does not exist for any active tectonic setting, including the western United States. Cycle skipping of surface waves is particularly problematic, so one could have the more realistic goal of eliminating time shifts for

periods >5 s. With dense data arrays and significant computational modeling, it is possible to fit the seismic wavefield at these periods. To integrate such a model into a moment tensor inversion would require replacing the inexpensive, efficient calculation of 1D synthetic seismograms with expensive calculation of 3D synthetic seismograms from wavefield simulations.

6. CONCLUSIONS

We present full moment tensor solutions, with uncertainties, for three sets of events: 21 earthquakes in southern Alaska, 63 events at Uturuncu volcano, Bolivia, and 29 events at the Nevada Test Site. We characterize each event as a point-source moment tensor with a fixed epicenter and origin time. The source time function is a trapezoidal function whose width scales with magnitude. We perform a separate grid search over depth and magnitude, and our emphasis on uncertainty estimation is with the 5D space of normalized moment tensors.

Our main findings are as follows:

1. The misfit function in moment tensor space exhibits local minima and other complexities (e.g., Figure 4). These reveal the importance of evaluating the misfit function over the full space of moment tensors, as opposed to linearized inversions, which may lead into an incorrect local minimum.
2. The complexities of the misfit function can be distilled into a confidence curve $P(V)$ that adjusts the posterior probability for the homogeneous probability of uniform moment tensors (Tape and Tape, 2016; Silwal and Tape, 2016). The area under the confidence curve is the confidence parameter P_{av} . Even in cases where moment tensor space is uniformly parameterized (e.g., Stahler and Sigloch, 2014), there is still a benefit to the confidence curve in that it can account for the ‘imprinted’ influence of the homogeneous probability for moment tensors.
3. We present a high-quality catalog of full moment tensors from the Nevada Test Site, building upon the efforts of Ford et al. (2009). In comparison with Ford et al. (2009), we include more stations, we use a lower minimum period (10 s) for all events, and we include (regional) body waves in all inversions. The inclusion of body waves improves the coverage of the source hemisphere, since the body-wave take-off angles tend to be steep (and downward), whereas surface-wave paths are near horizontal. Further efforts to include first-motion polarity measurements from short-period stations could result in moment tensor solutions with higher confidence than those presented here.

Additional work is needed to improve our understanding of the theory and application of moment tensor confidence curves. Most choices are made within the misfit function, which includes time windowing, weighting, choice of norm, and time shifting of synthetic seismograms. For example, a more complete representation of data covariance terms could eliminate the need for a scale factor. The use of 3D synthetic seismograms could lessen the need for time shifts, if the 3D velocity model is accurate. Some questions can be adequately addressed without real data within synthetic inversions.

Our primary goal has been to characterize uncertainties of moment tensors. This provides a starting point for interpreting the results in the context of physical models, such as those discussed in Tape and Tape (2013) or Patton and Taylor (2011). We can interpret any full moment tensor as a one-process model of an oblique opening crack (Minson et al., 2007) or as a two-process model of a tensional or compressional crack combined with shear slip within the same crack plane (Aki and Richards, 1980). More complex source processes have been proposed, but they cannot be distinguished or evaluated using the typical set of seismic waveforms.

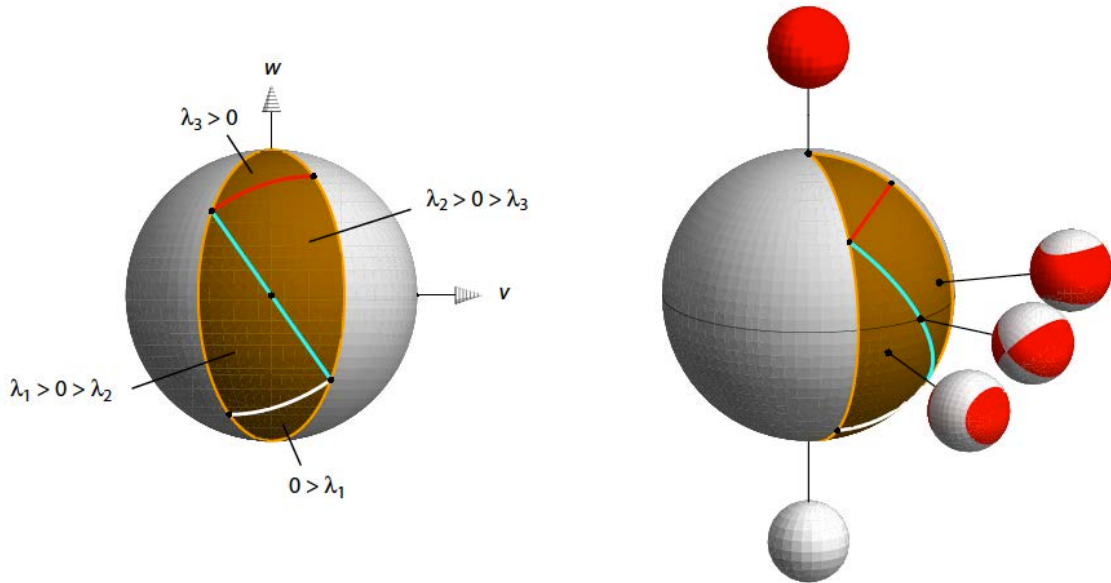


Figure 1. Fundamental lune for moment tensor source types. *Four regimes for moment tensors on the fundamental lune L . Above and to the right of the $\lambda_2 = 0$ (blue curve), moment tensor beachballs have red bands and white caps ($\lambda_2 > 0 > \lambda_3$). Below and to the left of it they have white bands and red caps ($\lambda_1 > 0 > \lambda_2$). Above the arc $\lambda_3 = 0$ (red), beachballs are all red ($\lambda_3 > 0$). Below the $\lambda_1 = 0$ (white), they are all white ($0 > \lambda_1$). (from Tape and Tape, 2013, Figure S1)*

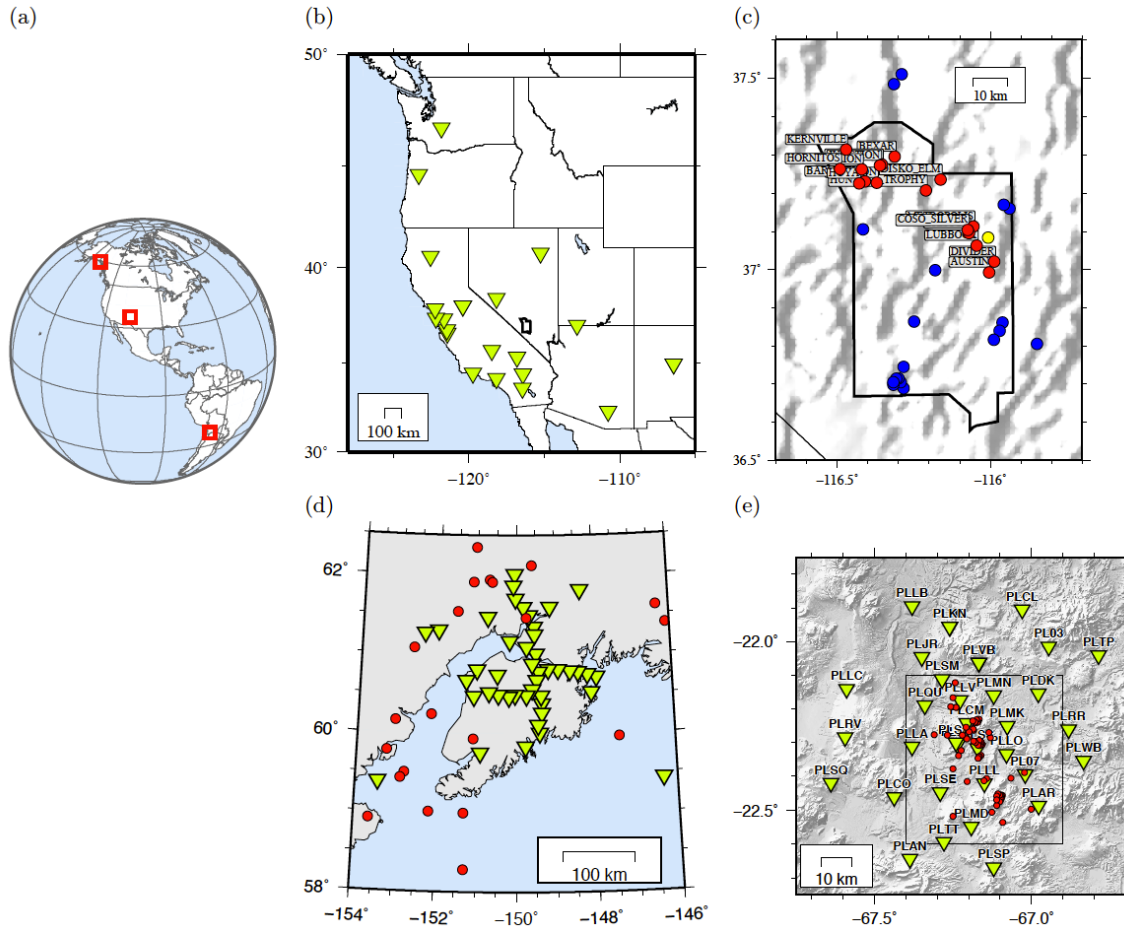


Figure 2. Locator maps for study regions. *Three study regions of the Nevada Test Site, Alaska, and Bolivia. (a) Global perspective showing our three study regions. (b) Western United States, showing Nevada Test site (outlined). (c) Zoom-in on Nevada Test Site. Nuclear explosions (17) are red, earthquakes (12) are blue, and collapses (3) are yellow. (d) 21 earthquakes in southern Alaska. (e) 63 events at Uturuncu volcano, Bolivia.*

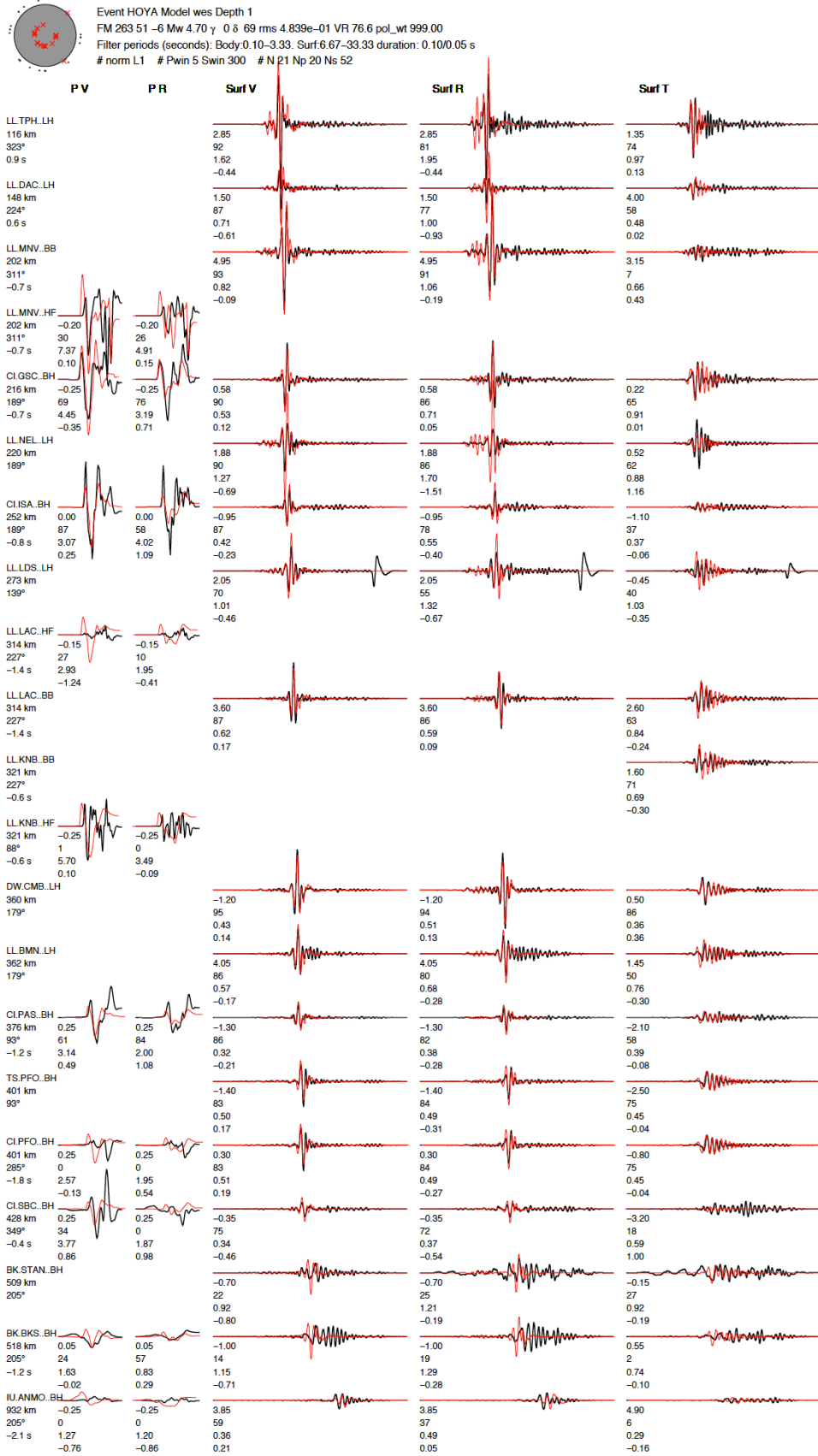


Figure 3. Waveform fits for HOYA nuclear test.

Approved for public release; distribution is unlimited.

Moment tensor solution and subset of waveform comparisons for the HOYA nuclear explosion. Each column is a different section of the three-component waveform: PV = vertical component P wave, PR = radial component P wave, SurfV = vertical component Rayleigh wave, SurfR = radial component Rayleigh wave, SurfT = transverse component Love wave. The stations are ordered by increasing epicentral distance from the top row. The observed waveforms are plotted in black, the synthetic waveforms are plotted in red. The body waves are filtered 3–10 Hz, and the surface waves are filtered 7–33 s. The numbers below each station name are the station epicentral distance (top) and station azimuth (bottom). The four numbers below each pair of waveforms are, from top to bottom, (1) the cross-correlation time shift $\Delta T = T_{obs} - T_{syn}$ required for matching the synthetics $s(t)$ with the data $u(t)$ (a positive time-shift means that the synthetics arrive earlier than the data); (2) the maximum cross-correlation percentage between $u(t)$ and $s(t - \Delta T)$; (3) the percentage of the total misfit; and (4) the amplitude ratio $\ln(A_{obs}/A_{syn})$ in each time window.

Event HOYA, M 4.70
 Lon -116.4290, Lat 37.2260
 Dep 0.7 km (inversion 1 km)
 Best source type γ 5°, δ 76°

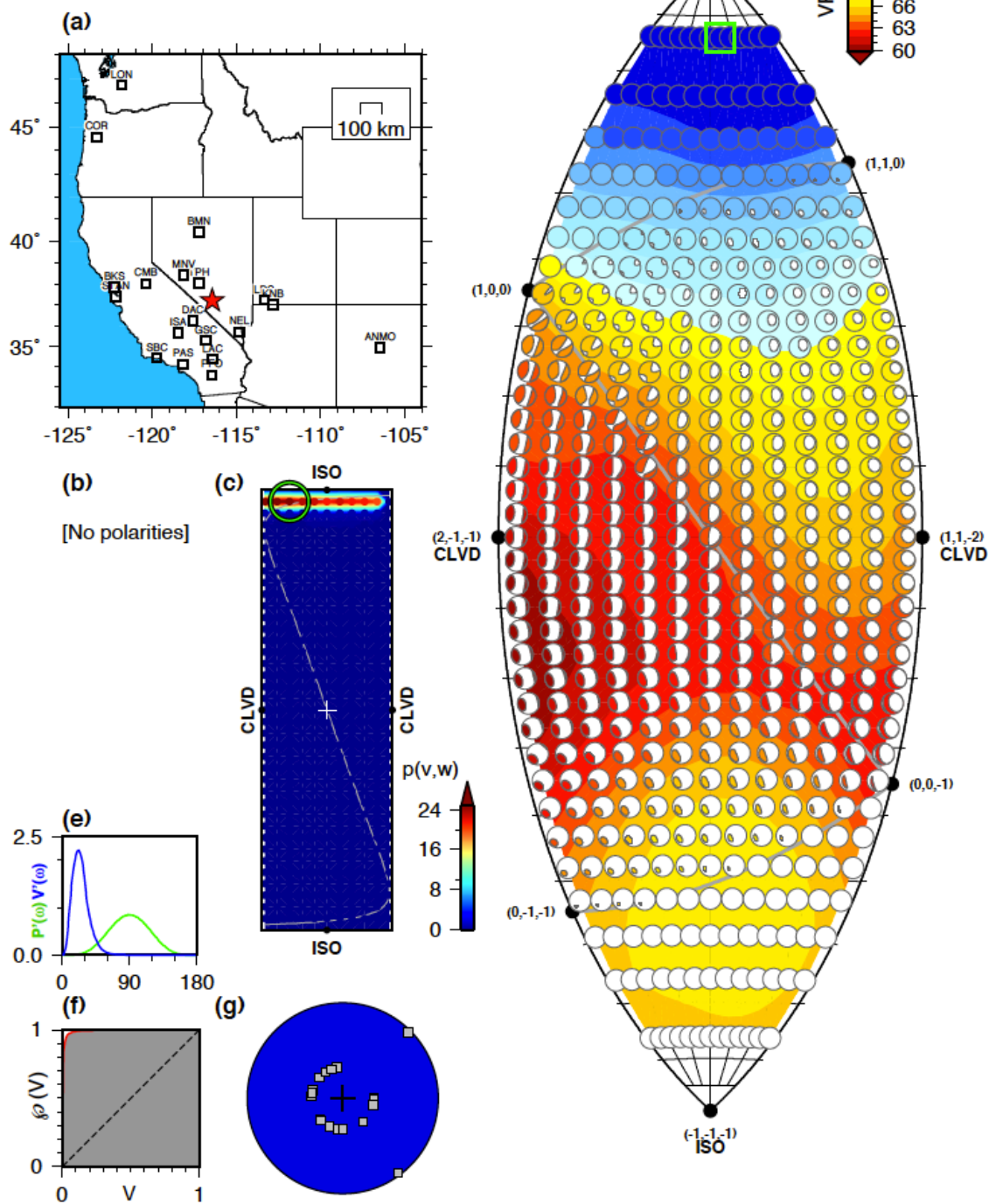


Figure 4. Uncertainty summary for HOYA nuclear test.

Waveforms for the best-fitting moment tensor are shown in Figure 3. (a) Map of source location (red star) and stations used in the inversion for this event. (b) Contour plot of the polarity misfit on the lune, if polarities are used, as in the case of the Uturuncu events (Alvizuri and Tape, 2016). (c) Probability density for moment tensor source type, plotted in vw space (Tape and Tape, 2015). A green circle indicates the location of the maximum. (d) Contour plot of the variance reduction $VR(\Lambda)$. The variance reduction $VR(\Lambda)$ at a point Λ is the maximum variance reduction $VR(M)$ for moment tensors M that have source type Λ and that have correct polarities. Large values (blue) of VR represent better fit between observed and synthetic waveforms. Of the beachballs $M(\Lambda)$, our desired solution M_0 (green box) is the one with largest VR . The gray arcs on the lune are the great circle arcs $\lambda_1 = 0$, $\lambda_2 = 0$, and $\lambda_3 = 0$ (white, cyan, and red in Figure 1). Selected eigenvalue triples (black dots) on the boundary of the lune are indicated, with the understanding that the triples need to be normalized. The positive isotropic source $(1, 1, 1)$ is at the top, the negative isotropic source $(-1, -1, -1)$ is at the bottom, and the double couple $(1, 0, -1)$, not shown, would be at the center of the lune. (e) Uniform and posterior probability curves with respect to ω , the angular distance from M_0 to a moment tensor. (f) Confidence curve $P(V)$ showing the distribution of probability as a function of fractional volume V . (g) The moment tensor M_0 , plotted in a lower-hemisphere projection. The location of the piercing point for each station depends on the station azimuth, epicentral distance, and the assumed layered reference model.

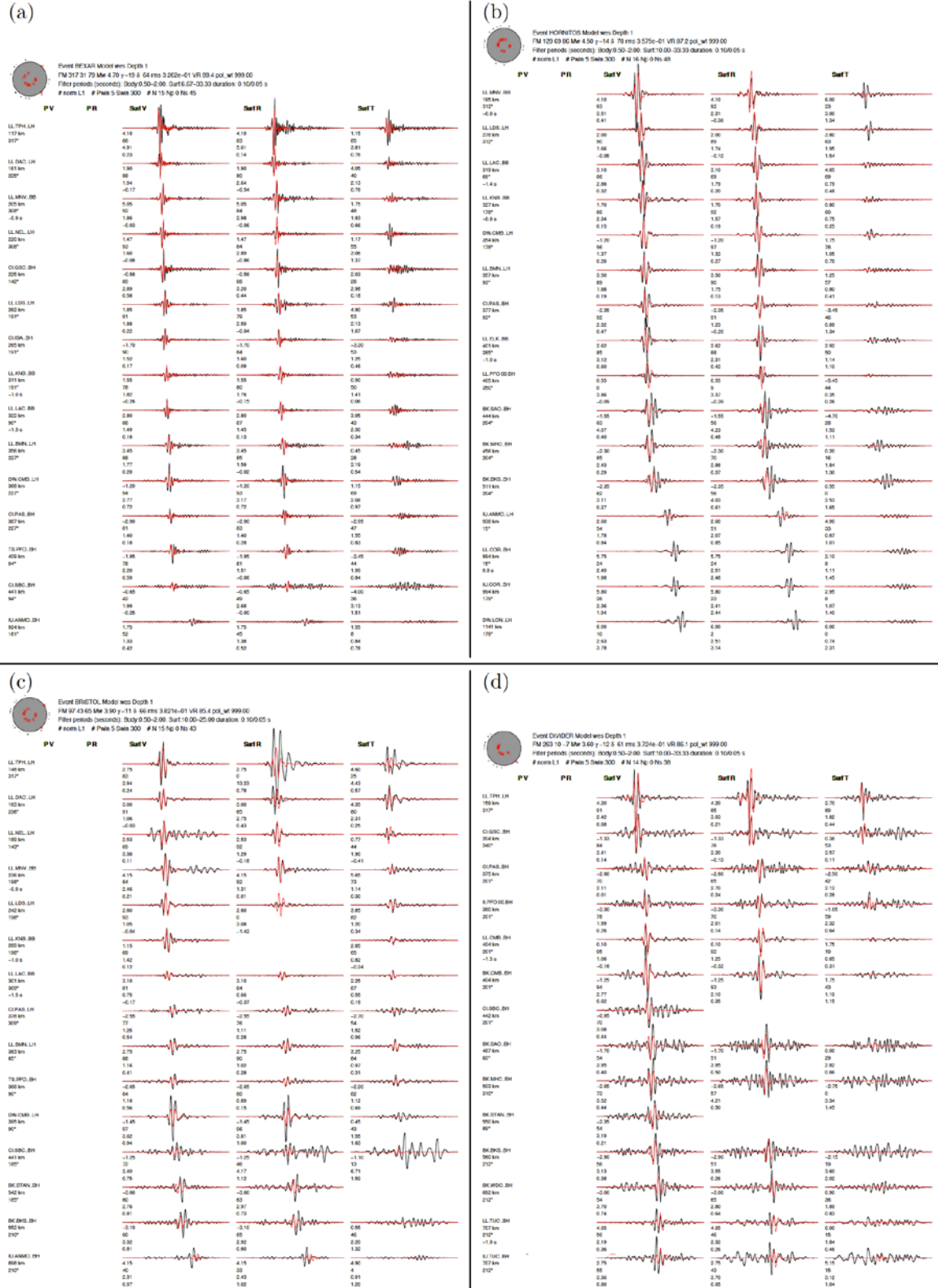


Figure 5. Waveform fits for four nuclear explosions. (a) BEXAR, (b) HORNITOS, (c) BRISTOL, and (d) DIVIDER. See Figure 6 for misfit plots on the lune.

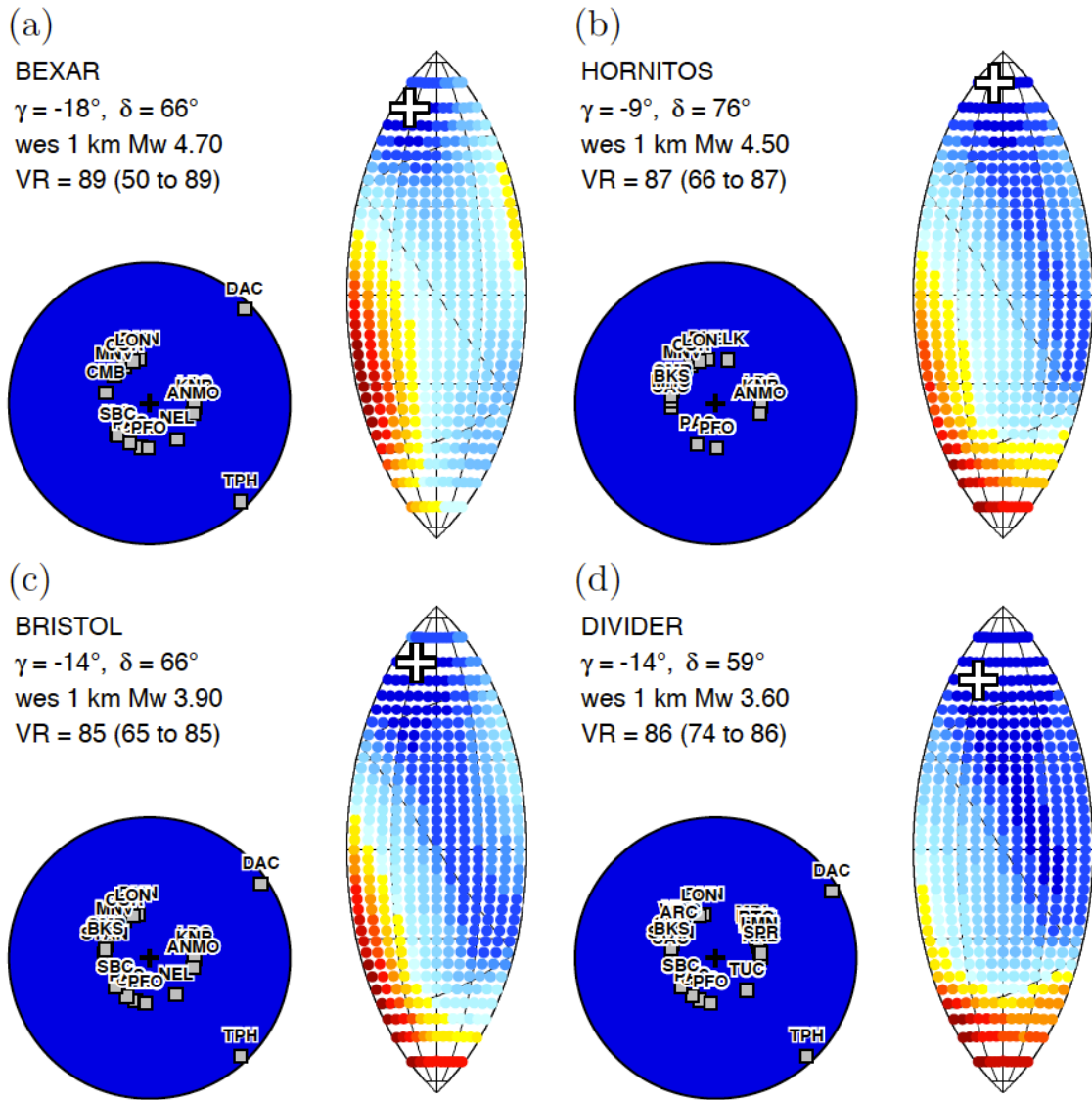


Figure 6. Lune plots for four nuclear explosions.

Misfit plots on the lune for four example nuclear explosions whose best-fitting waveform are shown in Figure 5. The color scale represents the variance reduction, from high (blue) at the best-fitting moment tensor, to low (red); the min/max values are adjusted in each subplot to show the variation on the lune.

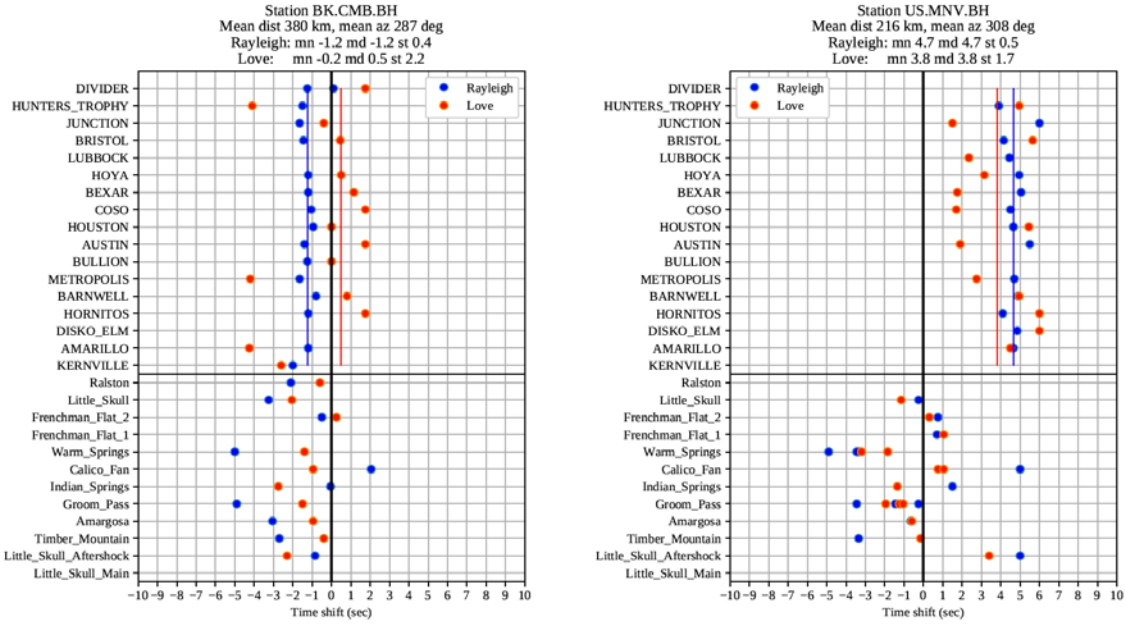


Figure 7. Surface wave time shifts for two examples stations (CMB and MNV) for all 17 nuclear explosions and all 12 earthquakes in our study.

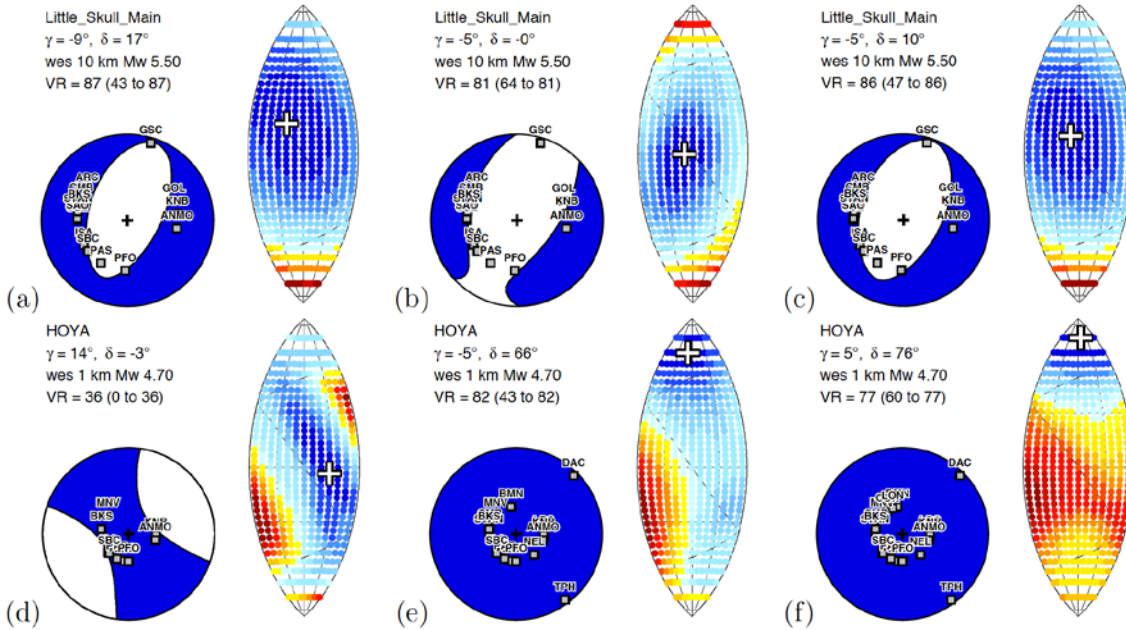


Figure 8. The influence of body waves on lune plots.

The influence of body waves and surface waves on moment tensor inversions for two example events. The color scale is adjusted for each subplot in order to show the variation in $VR(\Lambda)$. (a) Little Skull Mountain: body waves only; waveform fits in Figure S12. (b) Little Skull Mountain: surface waves only. (c) Little Skull Mountain: body and surface waves. (d) HOYA: body waves only. (e) HOYA: surface waves only.

(f) HOYA: body waves and surface waves; waveform fits in Figure 3, expanded version of uncertainty summary plot in Figure 4.

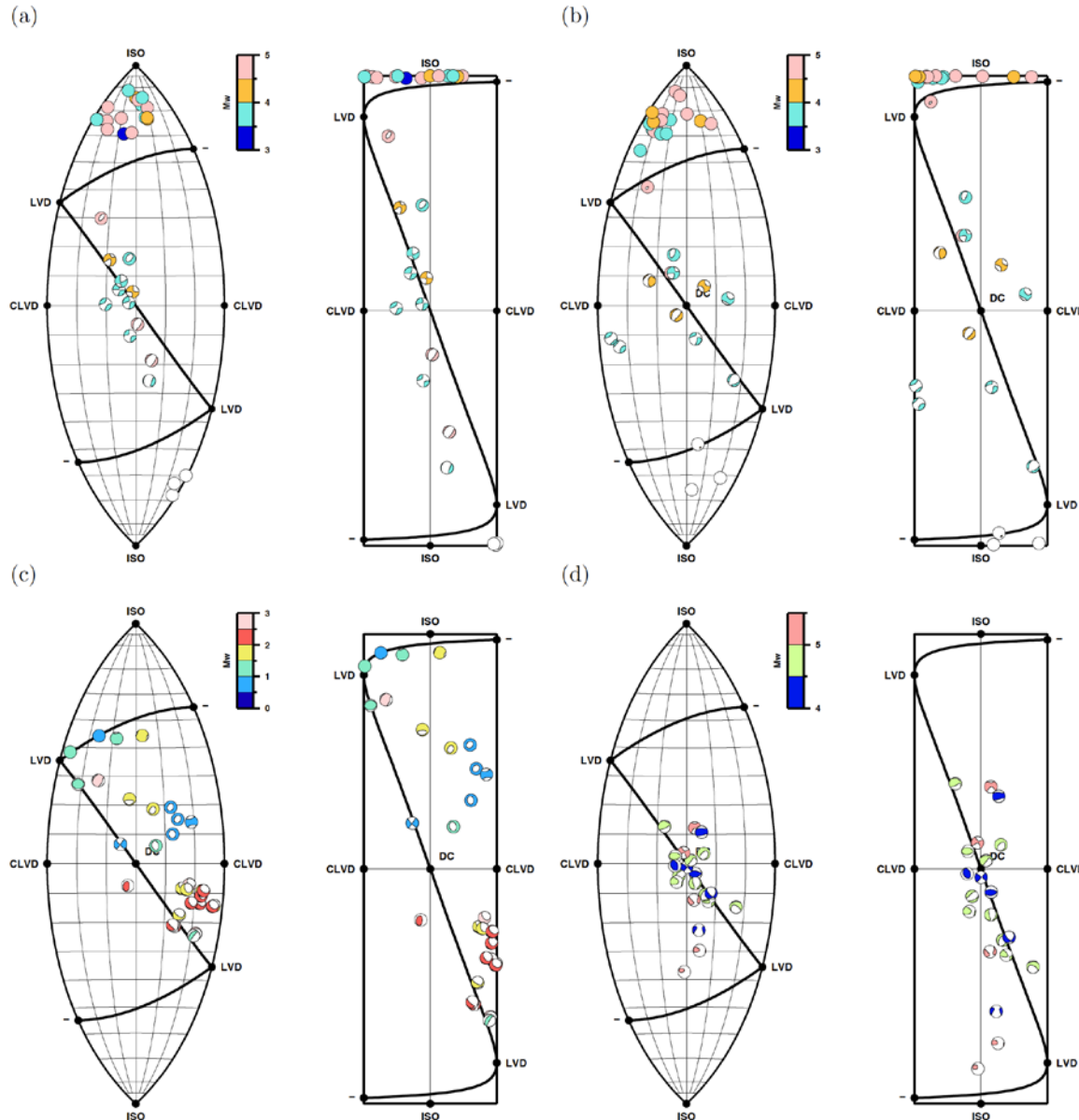


Figure 9. Moment tensor catalogs plotted on the lune.

Full moment tensor catalogs, plotted on the lune (left) and on the vw rectangle (right) (Tape and Tape, 2012, 2015). Beachballs are colored by magnitude. (a) 32 earthquakes, explosions, and collapses from the Nevada Test Site (Ford et al., 2009). (b) Same events as (a), but showing our solutions in this study. (c) 63 events from Uturuncu volcano, Bolivia. (d) 21 earthquakes from southern Alaska.

REFERENCES

(* denotes a publication from this project)

Aki, K. and P. G. Richards (1980), Quantitative Seismology, Theory and Methods, W. H. Freeman, San Francisco, CA, USA.

Alvizuri, C. and C. Tape (2016), Full moment tensors for small events ($M_w < 3$) at Uturuncu volcano, Bolivia, *Geophys. J. Int.*, 206, pp. 1761-1783, doi:10.1093/gji/ggw247.

*Alvizuri, C., V. Silwal, L. Krischer, and C. Tape (2016), Estimation of full moment tensors, including uncertainties, for earthquakes, volcanic events, and nuclear tests, Abstract S31A-2701 presented at 2016 Fall Meeting, AGU, San Francisco, CA, 12-16 December.

*Alvizuri, C., V. Silwal, L. Krischer, and C. Tape (2017), Estimation of full moment tensors, including uncertainties, for earthquakes, volcanic events, and nuclear explosions, Abstract T2.3-P8 presented at the CTBT Science and Technology Conference 2017, Vienna, Austria.

*Alvizuri, C., V. Silwal, L. Krischer, and C. Tape (2017, in prep.), Estimation of full moment tensors, including uncertainties, for nuclear explosions, volcanic events, and earthquakes, *J. Geophys. Res., Solid Earth*.

Boyd, O. S., D. S. Dreger, V. H. Lai, and R. Gritto (2015), A systematic analysis of seismic moment tensor at The Geysers geothermal field, California, *Bull. Seismol. Soc. Am.*, 105 (6), pp. 2969-2986, doi:10.1785/0120140285.

Ford, S. R., D. S. Dreger, and W. R. Walter (2009), Identifying isotropic events using a regional moment tensor inversion, *J. Geophys. Res.*, 114, B01306, doi:10.1029/2008JB005743.

Ford, S. R., D. S. Dreger, and W. R. Walter (2010), Network sensitivity solutions for regional moment tensor inversions, *Bull. Seismol. Soc. Am.*, 100(5A), pp. 1962-1970, doi:10.1785/0120090140.

Hudson, J. A., R. G. Pearce, and R. M. Rogers (1989), Source type plot for inversion of the moment tensor, *J. Geophys. Res.*, 94(B1), pp. 765-774.

Lohman, R. B., M. Simons, and B. Savage (2002), Location and mechanism of the Little Skull Mountain earthquake as constrained by satellite radar interferometry and seismic waveform modeling, *J. Geophys. Res.*, 107 (B6), doi:10.1029/2001JB000627.

Minson, S. E., D. S. Dreger, R. Burgmann, H. Kanamori, and K. M. Larson (2007), Seismically and geodetically determined nondouble-couple source mechanisms from the 2000 Miyakejima volcanic earthquake swarm, *J. Geophys. Res.*, 112, B10308, doi:10.1029/2006JB004847.

Patton, H. and S. Taylor (2011), The apparent explosion moment: Inferences of volumetric moment due to source medium damage by underground nuclear explosions, *J. Geophys. Res.*, 116, B03310, doi:10.1029/2010JB007937

Riedesel, M. A. and T. H. Jordan (1989), Display and assessment of seismic moment tensors, *Bull. Seismol. Soc. Am.*, 79(1), pp. 85-100.

Silwal, V. and C. Tape (2016), Seismic moment tensors and estimated uncertainties in southern Alaska, *J. Geophys. Res. Solid Earth*, 121, pp. 2772-2797, doi:10.1002/2015JB012588.

Stahler, S. C. and K. Sigloch (2014), Fully probabilistic seismic source inversion – Part 1: Efficient parameterisation, *Solid Earth*, 5, pp. 1055-1069, doi:10.5194/se-5-1055-2014.

*Tape, C. (2017a), Estimation of uncertainties of full moment tensors, Oral presentation at UCLA Institute of Physics and Applied Math Workshop II: Full Waveform Inversion and Velocity Analysis, Los Angeles, CA, 1-5 May.

*Tape, C. (2017b), Curves ($V_\gamma(\omega)$) (Tape and Tape, 2017) for download and details of their calculation, ScholarWorks@UA at <http://hdl.handle.net/11122/7234> (last accessed 2017-01-30): descriptor file, figures, and curves in ASCII format.

Tape, W. and C. Tape (2012a), A geometric setting for moment tensors, *Geophys. J. Int.*, 190, pp. 476-498, doi:10.1111/j.1365-246X.2012.05491.x.

Tape, W. and C. Tape (2012b), A geometric comparison of source-type plots for moment tensors, *Geophys. J. Int.*, 190, pp. 499-510, doi:10.1111/j.1365-246X.2012.05490.x.

Tape, W. and C. Tape (2012c), Angle between principal axes triples, *Geophys. J. Int.*, 191, pp. 813-831, doi:10.1111/j.1365-246X.2012.05658.x.

Tape, W. and C. Tape (2013), The classical model for moment tensors, *Geophys. J. Int.*, 195, pp. 1701-1720, doi:10.1093/gji/ggt302.

*Tape, W. and C. Tape (2015a), A uniform parameterization of moment tensors, *Geophys. J. Int.*, 202, pp. 2074-2081, doi:10.1093/gji/ggv262.

*Tape, W. and C. Tape (2015b), A uniform parameterization of moment tensors, Abstract S51A-2659 presented at 2015 Fall Meeting, AGU, San Francisco, CA, 14-18 Dec.

*Tape, W. and C. Tape (2016), A confidence parameter for seismic moment tensors, *Geophys. J. Int.*, 205, pp. 938-953, doi:10.1093/gji/ggw057.

*Tape, W. and C. Tape (2017), Volume in moment tensor space in terms of distance, *Geophys. J. Int.*, 210, pp. 406-419, doi:10.1093/gji/ggx164.

Walter, W. R., K. D. Smith, J. L. O'Boyle, T. F. Hauk, F. Ryall, S. D. Ruppert, S. C. Myers, R. Abbot, and D. A. Dodge (2006), An assembled western United States dataset for regional seismic analysis, ISSO 9660 CD, LLNL release UCRL-MI-222502.

Zhu, L. and Y. Ben-Zion (2013), Parameterization of general seismic potency and moment tensors for source inversion of seismic waveform data, *Geophys. J. Int.*, 194, pp. 839-843, doi:10.1093/gji/ggt137.

Zhu, L. and D. Helmberger (1996), Advancement in source estimation techniques using broadband regional seismograms, *Bull. Seismol. Soc. Am.*, 86(5), pp. 1634-1641.

DISTRIBUTION LIST

DTIC/OCP
8725 John J. Kingman Rd, Suite 0944
Ft Belvoir, VA 22060-6218 1 cy

AFRL/RVIL
Kirtland AFB, NM 87117-5776 1 cy

Official Record Copy
AFRL/RVBYE/Dr. Frederick Schult 1 cy